Accelerated Simulation of Multi-Electrode Arrays Using Sparse and Low-Rank Matrix Techniques

Nathan Jensen†*, Zhijie Charles Chen†, Anna Kochnev Goldstein, and Daniel Palanker

***Abstract*— Modeling of Multi-Electrode Arrays used in neural stimulation can be computationally challenging since it may involve incredibly dense circuits with millions of interconnected resistors, representing current pathways in an electrolyte (resistance matrix), coupled to nonlinear circuits of the stimulating pixels themselves. Here, we present a method for accelerating the modeling of such circuits while minimizing the error of a simplified simulation by using a sparse plus low-rank approximation of the resistance matrix. Specifically, we prove that thresholding of the resistance matrix elements enables its sparsification with minimized error. This is accomplished with a sorting algorithm implying efficient O (N log (N)) complexity. The eigenvalue-based low-rank compensation then helps achieve greater accuracy without adding significantly to the problem size. Utilizing these matrix techniques, we accelerated the simulation of multi-electrode arrays by an order of magnitude, reducing the computation time by about 10-fold, while maintaining an average error of less than 0.3% in the current injected from each electrode. We also show a case where acceleration reaches at least 133 times with additional error in the range of 4%, demonstrating the ability of this algorithm to perform under extreme conditions. Although the techniques presented here are used for simulations of photovoltaic retinal prostheses, they are also immediately applicable to any circuit involving dense connections between nodes, and, with modifications, more generally to any systems involving non-sparse matrices. This approach promises significant improvements in the efficiency of modeling the next-generation retinal implants having thousands of pixels, enabling iterative design with broad applicability.**

I. Introduction

Retinal prostheses show promise in restoring sight to patients impaired by retinal degeneration, such as age-related macular degeneration and retinitis pigmentosa. One such device that has shown particular success in clinical trials is the PRIMA photovoltaic subretinal system. The current PRIMA implant is 2 mm × 2 mm in size, corresponding to an approximately 7° field of view [1], filled with a hexagonal array of 100 µm wide pixels. The 100 µm gap between lines of a letter, such as a Tumbling E or Landolt C (LDC), corresponds to a visual acuity of 20/420 [2].

It has been demonstrated that grating acuity in rodents matches the pixel size of subretinal photovoltaic implants, up to their natural resolution limit of 28 µm [3]–[5]. It would follow that to increase the resolution in patients beyond 20/420, the size of individual pixels should be decreased (ideally up to 5 µm for 20/20 vision); and to widen the field of view, the implant width should be increased up to some anatomical constraints – such as a size of the geographic atrophy in AMD patients, retinotomy length, etc. Predicting the electric field in electrolyte generated by smaller pixels in a larger array requires an accurate modeling framework for such an implant. For this purpose, the Retinal Prosthesis Simulator (RPSim) has been developed [6].

RPSim is a platform for calculating the electric field in tissue (an electrolytic medium) generated by a multi-electrode array, each pixel of which may include an electric circuit [6]. It does so by coupling the power of finite element method (FEM) physics modelling with the efficiency of SPICE-based circuit solvers. For these respective tasks, RPSim relies on COMSOL Multiphysics® [7] and XYCE, a SPICE-like circuit solver developed by Sandia National Laboratories [8]. First, the elementary field of an electrode and resistance of the medium between the electrodes are calculated with FEM, and then the results are used to build an accurate circuit model, which includes all pixels coupled to a common electrolyte via their electrodes. The circuit model provides the dynamics of an electric current in each pixel, which is then used to calculate the resulting electric field in the medium as a sum of the elementary fields from each electrode, weighted by its respective current.

With the modeling performed in RPSim, the number of computations increases quadratically with the number of pixels on such a photovoltaic array due to a cross-coupling between each electrode in the model. The number of electrodes depends on both the pixel size and the implant dimensions. For example, with 20 µm pixels on a 3 mm wide implant, the number of pixels exceeds 20,000 and the number of resistors in a mesh representing the electrolyte exceeds 4×10^8. As pixels get smaller, and the implant – larger, computations quickly become unattainably long, and require an incredibly large operating memory, which prevents efficient modelling of

Submitted for review July 29, 2024. Studies were supported by the National Institutes of Health (R01-EY-035227 and P30-EY-026877) and the Department of Defense (W81XWH-22-1-0933). † The first two authors contributed equally to this work. * *Corresponding author*

Nathan Jensen is with the Department of Electrical Engineering, Stanford University, Stanford, CA 94305 USA (e-mail: njensen@stanford.edu).

Zhijie Charles Chen was with the Department of Electrical Engineering, Stanford University, Stanford, CA 94305 USA

Anna Kochnev Goldstein, is with the Department of Electrical Engineering, Stanford University, Stanford, CA 94305 USA

Daniel Palanker is with the Department of Ophthalmology and Hansen Experimental Physics Laboratory, Stanford University, Stanford, CA 94305 USA

the next-generation implants.

As mentioned, to solve the circuit dynamics involved in a neurostimulating array, RPSim relies on the circuit solver Xyce [6], [8]. One would be hard pressed to develop a tool that can outperform such a mature and proven simulator, capable of handling millions of circuit elements. However, these solvers have been developed using a node-based approach and optimized under the assumption that the matrix between adjacent nodes is sparse. This assumption breaks down for mutually coupled multi-electrode arrays that suffer from an extremely dense conductance matrix. To help, one can find a sparse matrix approximation, but the error introduced by such a technique can be very large. We can, however, reduce this error by using low rank compensation matrices. To the author's knowledge, circuit solvers, such as Xyce, have no such built-in methods to increase their computational efficiency. Instead, for such large-scale problems they suggest the user rely on parallel computing and iterative methods, such as Krylov, which require a well-designed and problem-specific preconditioner for good performance [9]–[11]. Here, we present a much simpler and more astute alternative to such complicated algorithms for reducing the computational intensity of modeling a large mesh network of photovoltaic pixels connected via a common electrolyte. This approach is generalizable to other massive electronic circuits coupled to an electrolyte or another conductive medium.

II. Methods

A. Sparse Approximation

The photovoltaic multielectrode array used in a subretinal implant, such as PRIMA, consists of tiled hexagonal pixels, each of which has one or more photodiodes connected between the active and return electrodes (Fig. 1). Active electrodes are at the center of the pixels, while return electrodes cover the edges of each pixel, connected together over the whole mesh [6]. These photodiodes convert near-infrared light projected from the augmented reality glasses into electric current, which is injected into the retina to stimulate the nearby neurons [1]. All pixels are coupled to each other via a conductive (electrolytic) medium, as shown in Fig. 1, and thus each affects the electrical dynamics of all others. Consider the effects of the pixel 2 – which we will briefly assume has a hemispherical electrode injecting a current I_2 while all other pixels remain idle. A hemispherical electric field will form in the medium, resulting in an elevated electric potential: $\Delta V \approx (I_2 \cdot \rho)/(2\pi l)$, where l is the distance from the center of that electrode and ρ is resistivity of the medium. Using this, we can characterize the conductive medium as an ohmic resistance between the active pixel 2 and another pixel i, which is inversely proportional to the distance between their centers $l_{i,2}$

$$R_{i,2} := \frac{\Delta V_{i,2}}{I_2} = \frac{\rho}{2\pi l_{i,2}}$$

Or more generally,

$$R_{i,j} := \frac{\Delta V_{i,j}}{I_j} \approx \frac{\rho}{2\pi l_{i,j}} \tag{1}$$

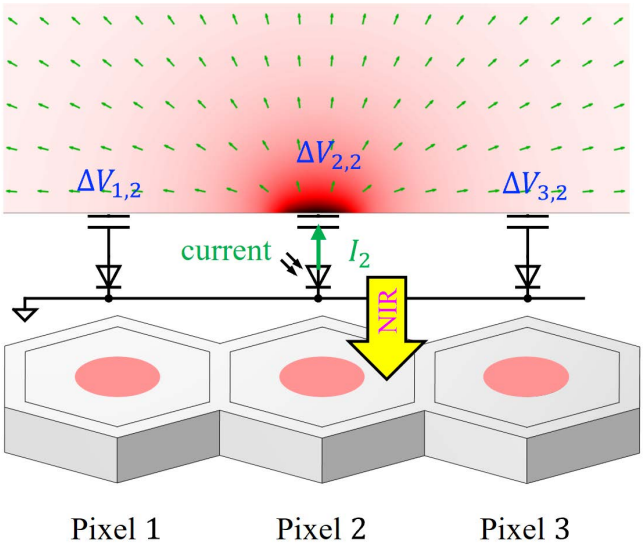

Fig. 1: Illustration of the cross-pixel potential coupling of multiple electrodes in electrolyte. The center pixel is illuminated and injects a current I_2.

For an adjacent pixel 1, $l_{1,2}$ would be on the order of the pixel width W. Additionally, for the "self-resistance" of a pixel $R_{j,j} = \Delta V_{j,j}/I_j \approx \rho/(4r)$, where r is the electrode radius – following the conventional definition for access resistance of the disk electrode [12]. Furthermore, due to linearity of the conductive medium, when multiple pixels inject current simultaneously, the potential rise ΔV at pixel j is simply the sum of all the potentials calculated individually, i.e. superposition. This formulation allows modelling the cross-coupling of all N electrodes as a mesh network of resistors in matrix form [3], [6].

$$\mathbf{R} := \begin{bmatrix} R_{1,1} & R_{1,2} & \cdots & R_{1,N} \\ R_{2,1} & R_{2,2} & & \\ \vdots & & \ddots & R_{N-1,N} \\ R_{N,1} & & R_{N,N-1} & R_{N,N} \end{bmatrix} \tag{2}$$

By reciprocity of electromagnetism, this matrix will be symmetric. The size of this resistor mesh scales quadratically with the number of pixels, and hence it scales to the fourth power with both the implant width as well as the inverse of the pixel size. Consequently, the computational workload of simulating such a mesh grows accordingly for both factors. This mesh is the primary contributing factor to the polynomial relationship between computational complexity and the number of pixels on an implant.

The problem of reducing the computational complexity can be framed as finding a matrix which approximates the conductance matrix $\mathbf{G} := \mathbf{R}^{-1}$, but is in some way computationally lighter. For example, one may find a sparse approximation, denoted as $\mathbf{S}$. Because of the spatial dependence of $R_{i,j}$ – being inversely proportional to $l_{i,j}$ – one intuitive method of sparsification would be to find some threshold value for the distance between two electrodes, such that their coupling is so small it can be neglected, i.e. set to 0 in the conductance matrix. However, the total number of coupled electrodes, η,

some distance $l_{i,j}$ away from the center electrode is roughly proportional to $l_{i,j}$

$$\eta \approx \frac{2\pi \cdot l_{i.j}}{W} \tag{3}$$

The variable $l_{i,j}$ in (2) and (3) cancels out, such that the overall contribution to the effective access resistance of one electrode from consecutive rings of neighboring electrodes is largely constant with distance. Therefore, this naïve thresholding alone can result in a very large error, which will be addressed later. Formally, one needs to find a sparse approximation $\mathbf{S}$ for the network $\mathbf{G}$ with no more than k non-zero entries, such that $\mathbf{S}$ is positive definite and the error

$$\mathbf{E} := \mathbf{G} - \mathbf{S} \tag{4}$$

is minimized, where k is a value dependent on the computational resources available. To minimize the error, which is expressed in matrix form here, we will minimize the spectral energy— defined as the sum of squares of all the eigenvalues of $\mathbf{E}$, which for a symmetric matrix is equivalent to the square of the Frobenius norm of $\mathbf{E}$.

$$\sum \lambda^2(\mathbf{E}) = \|\mathbf{E}\|_{\text{fro}}^2 := \sum_{m,n} \mathbf{E}_{m,n}^2, \tag{5}$$

where $()_{m,n}$ denotes the entry in the mth row and the nth column of a matrix. Therefore, combining (4) and (5), this can be written as the optimization problem:

$$\begin{aligned} \min_{\mathbf{S}} \quad & \sum \lambda^2(\mathbf{G} - \mathbf{S}) \\ \text{s.t.} \quad & \|\mathbf{S}\|_0 \leq k, \\ & \mathbf{S} \succ 0. \end{aligned} \tag{6}$$

This problem has a direct solution, which does not require iteration to solve. Let I^+ be a set comprising all indices (m, n) such that $\mathbf{S}_{m,n} \neq 0$, and having complementary set $I^- := \{(m, n) | \mathbf{S}_{m,n} = 0\}$. Note that

$$\sum_{m,n} \mathbf{E}_{m,n}^2 = \sum_{(m,n)\in I^-} \mathbf{E}_{m,n}^2 + \sum_{(m,n)\in I^+} \mathbf{E}_{m,n}^2, \tag{7}$$

and for $(m, n) \in I^-, \mathbf{E}_{(m,n)} = \mathbf{G}_{(m,n)}$. From this One has:

$$\sum_{m,n} \mathbf{E}_{m,n}^2 \geq \sum_{(m,n)\in I^-} \mathbf{G}_{m,n}^2, \tag{8}$$

where the equality is achieved if and only if $\mathbf{S}_{m,n} = \mathbf{G}_{m,n}$ for all $(m, n) \in I^+$. In this case,

$$\sum \lambda^2(\mathbf{E}) = \sum_{m,n} \mathbf{E}_{m,n}^2 = \sum_{(m,n)\in I^-} \mathbf{G}_{m,n}^2. \tag{9}$$

The solution to this optimization is indeed found by thresholding $\mathbf{G}$ by it's k^{th} largest entries, as postulated above, and setting all other values in $\mathbf{G}$ to be 0. Therefore, the solution can be found with a sorting algorithm in time $O(N \log(N))$.

If we define a column vector of the potential at each pixel as $\boldsymbol{V}$, then from multidimensional Ohm's Law, we can use the error in the conductance matrix, $\mathbf{E}$, to define the vector containing the error in injected current for each pixel as $\boldsymbol{I}_{\text{err}} := \mathbf{E}\boldsymbol{V}$. This error is therefore bounded by:

$$\frac{\|\boldsymbol{I}_{\text{err}}\|}{\|\boldsymbol{I}\|} = \frac{\|\mathbf{E}\boldsymbol{V}\|}{\|\mathbf{G}\boldsymbol{V}\|} \leq \frac{\max|\lambda(\mathbf{E})|}{\min|\lambda(\mathbf{G})|}. \tag{10}$$

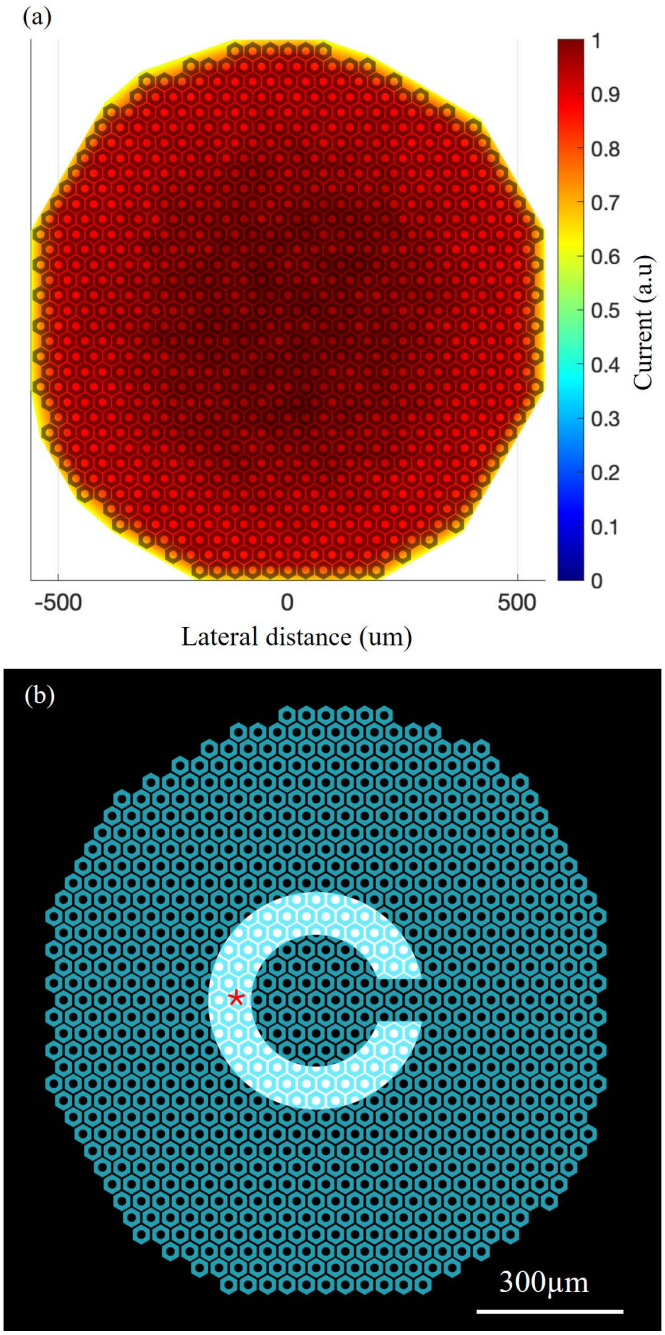

Fig. 2: (a) Map of the principal component of the error matrix $\mathbf{E}$ resulting from thresholding out 90% of the smallest magnitude entries of $\mathbf{G}$, the corresponding conductance matrix for a 40 µm monopolar implant. Values are normalized by the largest entry. (b) A Landolt C pattern with a 90 µm wide gap projected onto the array. The red asterisk labels the pixel whose current is plotted in Fig. 5(a).

B. Low Rank Compensation

By this metric, the maximum eigenvalue in $\mathbf{E}$ contributes the most to the current error, and because of this, error might be decreased by compensating for the specific terms in $\mathbf{E}$. The largest eigenvalue of $\mathbf{E}$ represents the principal component of the error – and represents a relatively uniform current

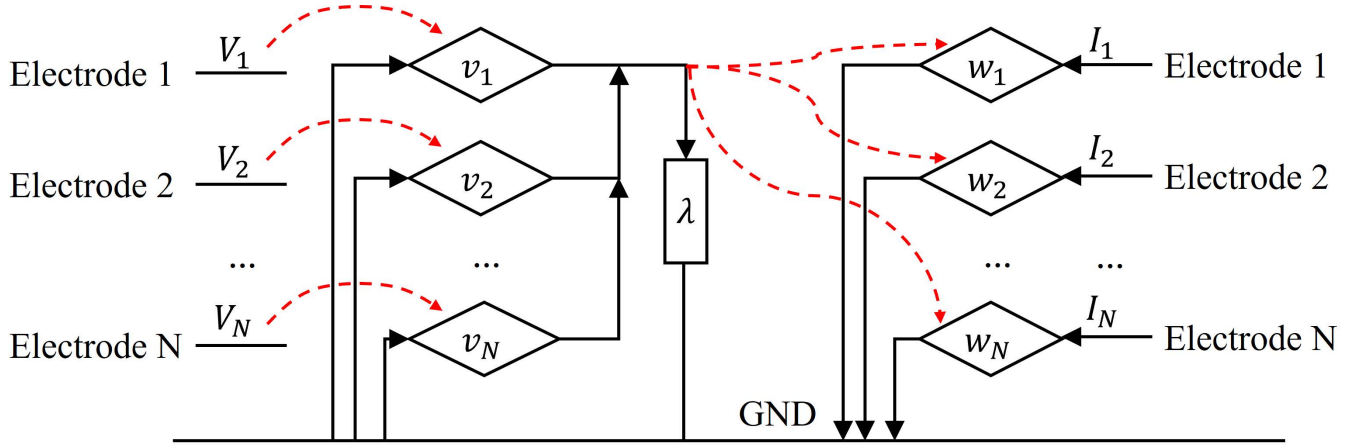

Fig. 3: Circuit level implementation of a rank-1 compensation to a sparse conductance matrix. The red dash arrows indicate where each voltage-controlled current source (diamond) takes the control signal from, and the rectangle labeled λ is a resistor.

profile caused by the error of neglecting small-magnitude couplings between distant electrodes, as was discussed. This error is approximately the same for each electrode in the array, albeit slightly different for electrodes closer to the edge of the implant that have fewer close neighbors. To correct this, a simple error-reduction technique will be introduced and deemed general compensation since the error from these principal components does not involve any information about which electrodes are injecting current. This compensation is achieved through the addition of a low rank matrix to the sparse matrix $\mathbf{S}$ and having error $\mathbf{E}_1$:

$$\mathbf{S}_1 = \mathbf{S} + \sum_{m=1}^{M} \boldsymbol{u}_m \lambda_m \boldsymbol{u}_m^\intercal, \tag{11}$$

$$\mathbf{E}_1 = \mathbf{G} - \mathbf{S}_1 = \mathbf{E} - \sum_{m=1}^{M} \boldsymbol{u}_m \lambda_m \boldsymbol{u}_m^\intercal. \tag{12}$$

where $\mathbf{S}_1$ is the resulting compensated matrix, λ_m is the mth largest eigenvalue of $\mathbf{E}$, and $\boldsymbol{u}_m$ is the corresponding eigenvector. M is thus the total number of desired compensation vectors, which can be as large as the number of eigenvalues in the error matrix $\mathbf{E}$. By definition, this will be at most the number of electrodes N. As M increases, the total error will decrease at the cost of a larger compensation matrix. The resulting compensation mode from the principal component is largely uniform as thresholding removes a similar number of interconnects for each electrode, removal of which results in the equivalent resistance of an electrode being too high. To rectify that, the compensation must provide additional conductivity to the electrode. On the edges of the array, less interconnects are removed from the matrix and thus less added conductivity is needed. This gives rise to the pattern shown in Fig. 2(a).

Further specific compensation terms can be added with knowledge of the illumination patterns of interest or the operation mode of the implant, such as if there is no forward conduction through the diodes, which is called a current limited regime [14]. For example, if a known pattern is projected, resulting in an expected photocurrent in each pixel $\boldsymbol{I}_{pho}$, then the expected voltage distribution can be calculated as $\boldsymbol{v} = \mathbf{G}^{-1}\boldsymbol{I}_{\text{pho}}$, assuming that the device operates under current limited conditions. The corresponding current error is $\boldsymbol{w} = \mathbf{E}_1\boldsymbol{v}$. Since $\boldsymbol{v}$ constitutes the primary voltage mode from the pattern, $\boldsymbol{w}$ will be the primary current error. Therefore, we can add the following specific compensation:

$$\mathbf{S}_2 = \mathbf{S}_1 + \frac{1}{\|\boldsymbol{v}\|}\boldsymbol{w}\boldsymbol{v}^\intercal. \tag{13}$$

This image-specific compensation is generalizable such that successive low-rank compensations can be added for a variety of illumination patterns and implant operation conditions.

C. Circuit Implementation

In RPSim, the conductance matrix is implemented as a mesh network of resistors. With a sparse matrix, we can eliminate some resistors from the model, and as such, implementation involves simply replacing $\mathbf{G}$ with $\mathbf{S}$. However, it would be counterproductive to replace $\mathbf{G}$ with $\mathbf{S}_1$ or $\mathbf{S}_2$ as the compensation terms are not sparse. They are low rank, but SPICE based circuit solvers do not have support for low-rank representation of matrices. Thus, maintaining computational efficiency while introducing compensation terms requires a means of adding a low-rank matrix to a sparse one without sacrificing the sparsity. This can be accomplished in Xyce through the addition of several additional nodes.

Let the rank-1 compensation matrix be $\boldsymbol{w}\lambda\boldsymbol{v}^\intercal$. The implant has N electrodes, including the active electrodes and the return units. $\boldsymbol{w} = [w_1, w_2, \cdots, w_N]^\intercal$ and $\boldsymbol{v} = [v_1, v_2, \cdots, v_N]^\intercal$ are N-dimensional vectors. For the general compensation, $\boldsymbol{w} = \boldsymbol{v}$; for the specific compensation, $\lambda = 1/\|\boldsymbol{v}\|$. One may implement the compensation $\boldsymbol{w}\lambda\boldsymbol{v}^\intercal$ with $2N$ voltage-controlled current sources (VCCSs) and a resistor, as illustrated in Fig. 3. Each VCCS in the left group takes voltage control from an electrode, multiplies the voltage with the corresponding entry in $\boldsymbol{v}$, and adds the current to a resistor λ. The voltage at the top node of the resistor is $\lambda\boldsymbol{v}^\intercal\boldsymbol{V}$. The VCCSs in the right group then take the voltage from the top node of λ, multiply it with $\boldsymbol{w}$, and pull the corresponding currents from the same set of

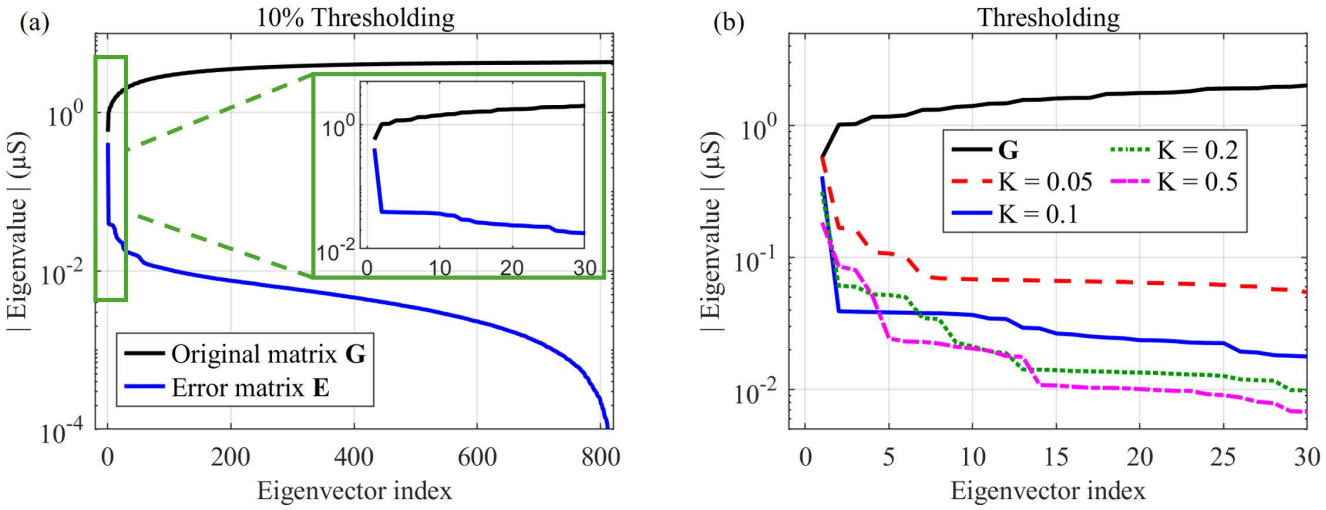

Fig. 4: Eigenvalues of the conductance matrix $\mathbf{G}$ sorted by ascending magnitudes, and those of the error matrix $\mathbf{E}$ by descending magnitudes, $\mathbf{E} = \mathbf{G} - \mathbf{S}$. The relative error is bounded by the inverse of the gap between the two spectra. (a) $\mathbf{S}$ is a sparse approximation of $\mathbf{G}$ with $\mathrm{K} = 0.1$, the parameter used for simulations in this paper. (b) The error spectrum is shown for several values of K.

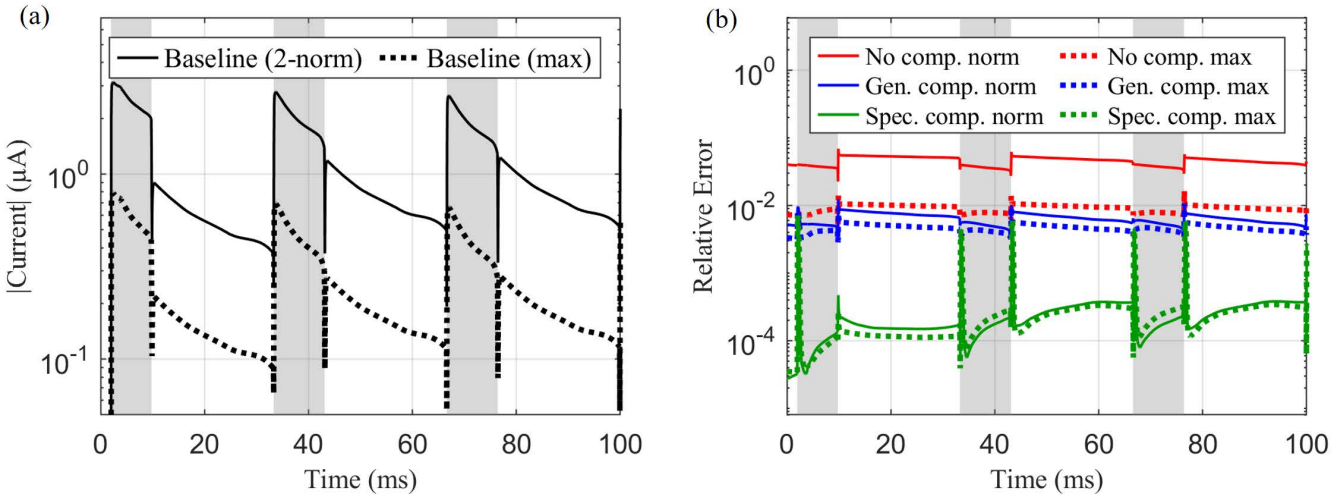

Fig. 5: Currents on the implant across time for the stimulation shown in Fig. 2, the shaded portion indicates the times when the stimulation pattern is turned on. (a) Baseline calculated with unmodified full matrix. Maximum current injected from the pixel shown in Fig. 2(b) (max) and the 2-norm of the currents of all pixels. (b) Relative error of the pixel shown in Fig. 2(b) (max) and the 2-norm of the error of the currents for all pixels: for the uncompensated matrix, with general compensation, and with image-specific compensation.

electrodes 1 to N. The coupled $i - v$ relationship between all electrodes is given by

$$\boldsymbol{I} = \boldsymbol{w}\lambda\boldsymbol{v}^{\intercal}\boldsymbol{V}. \tag{14}$$

This approach can implement a rank-1 compensation matrix $\boldsymbol{w}\lambda\boldsymbol{v}^{\intercal}$ in Xyce, using only $2N + 1$ elements and one additional node, instead of the $(N(N-1))/2$ resistors otherwise required by the full resistor mesh. For a more formal proof of this concept, consider a $N \times N$ sparse matrix $\mathbf{S}$ and a rank-L compensation term $\mathbf{W}\mathbf{\Lambda}\mathbf{V}^{\intercal}$, where $\mathbf{W}$ and $\mathbf{V}$ have dimensions of $N \times L$, $\mathbf{\Lambda}$ is a $L \times L$ diagonal matrix, and $L \ll N$. Rather than explicitly solving a linear system with an unknown vector variable $\boldsymbol{x}$ and a known vector $\boldsymbol{b}$:

$$(\mathbf{S} + \mathbf{W}\mathbf{\Lambda}\mathbf{V}^{\intercal})\,\boldsymbol{x} = \boldsymbol{b}, \tag{15}$$

which enjoys neither sparsity nor low-rankness, one can instead solve the following system with L additional dimensions:

$$\begin{bmatrix} \mathbf{S} & \mathbf{W} \\ \mathbf{V}^{\intercal} & -\mathbf{\Lambda}^{-1} \end{bmatrix} \begin{bmatrix} \boldsymbol{x} \\ \boldsymbol{y} \end{bmatrix} = \begin{bmatrix} \boldsymbol{b} \\ \boldsymbol{0} \end{bmatrix}. \tag{16}$$

The augmented equation above requires

$$\begin{cases} \mathbf{S}\boldsymbol{x} + \mathbf{W}\boldsymbol{y} = \boldsymbol{b}, & \text{(17a)} \\ \mathbf{V}^{\intercal}\boldsymbol{x} - \mathbf{\Lambda}^{-1}\boldsymbol{y} = \boldsymbol{0}. & \text{(17b)} \end{cases}$$

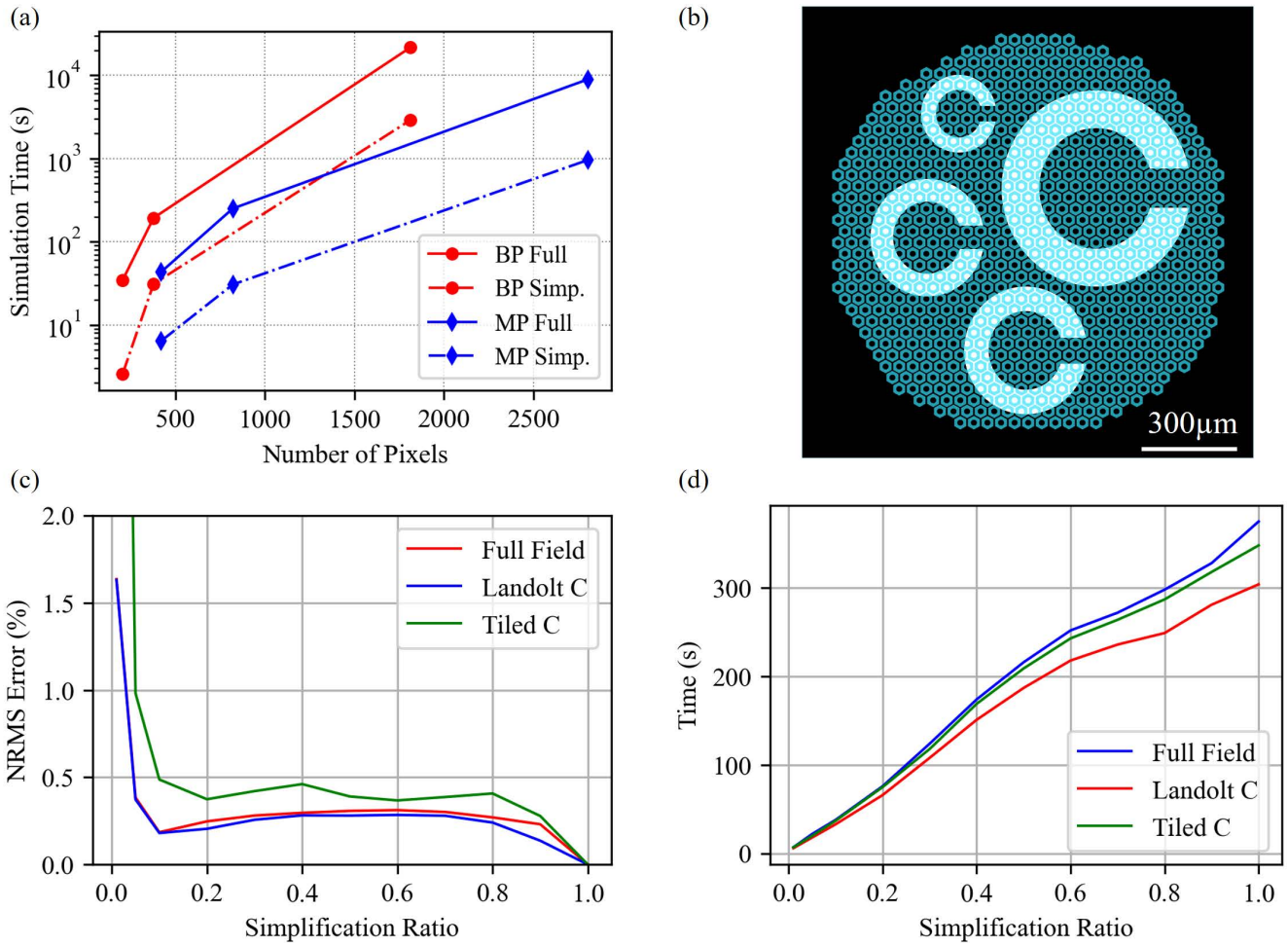

Fig. 6: (a) Simulation time for the full conductance matrix and the simplified and compensated matrix. (b) 'Tiled C' pattern used in (c) and (d), 'Landolt C' is shown in Fig. 2(b) and 'Full Field' means all pixels are uniformly illuminated. (c) Error for various patterns as a function of a simplification ratio K. (d) Simulation time as a function of K for various patterns.

Equation (17b) gives:

$$\boldsymbol{y} = \boldsymbol{\Lambda}\mathbf{V}^{\intercal}\boldsymbol{x}. \tag{18}$$

Substituting the above $\boldsymbol{y}$ into (17a) results in (15), while the matrix in (16) maintains its sparsity, demonstrating the validity of such an approach.

D. Additional Considerations

Further simplifications of the circuit can be made under certain conditions. For example, under low irradiances when the implant operates in the current limited regime, the voltage across the parallel diode used in a conventional model of a photodiode will be below the threshold of forward diode conduction. In this case, the forward current through the diode will be negligible and we can model the diode as an open circuit without sacrificing accuracy. This is advantageous as diodes are the only non-linear component in the circuit and removing them can significantly increase the computation speed. This technique can be especially useful for modelling larger photovoltaic arrays with smaller pixels at low irradiances. However, this assumption will quickly break down at high irradiances when the diodes begin to conduct. In the context of subretinal implants, the maximum irradiance level before this occurs also depends on the number of diodes in series within a pixel, typically ranging from 1 to 3 [13].

III. Results and Discussion

For demonstration purposes, a 1.5 mm implant composed of $N = 821$ hexagonal 40 µm wide monopolar pixels was modelled. For sparsification, the thresholding value k was set in a ratiometric manner with the ratio K, such that $k = \|\mathbf{G}\|_0 \cdot \mathrm{K}$. Here, K was set to 0.1, which corresponds to keeping 10% of the initial entries of $\mathbf{G}$ – or a 90% reduction in size of the resistor mesh. Recall that error is bounded by the maximum eigenvalue of $\mathbf{E}$ divided by the minimum eigenvalue of $\mathbf{G}$ (10), plotted in Fig. 4(a). The initial bound on the error – (10) evaluated at the first eigenvalue in Fig. 4(a) – is about 70%. However, this error can be dramatically improved by compensating for just the first principal component of the error. In this case, after implementing the general compensation with the eigenvector associated with the largest eigenvalue of $\mathbf{E}$ ($M =$

1), the error will be bounded by the second largest eigenvalue in $\mathbf{E}$, with an error of less than 7%. This demonstrates that we can improve the bounded error by an order of magnitude by adding a rank one compensation matrix, which corresponds to $2N + 1$ circuit elements. Doing so dramatically reduced the super-linear scaling in computational time, such that one can choose an acceptable error and runtime. With these parameters, the original netlist size was 13 MB, while after simplification and compensation it decreased to 1.7 MB. It is important to note that the error spectrum in Fig. 4 depends on the implant geometry as well as the value of K. In some cases, more than the first principal component must be included to achieve an acceptable error, at the cost of adding a corresponding number of circuit elements to the simulation, as illustrated in Fig. 4(b). Notably, for certain values of M, choosing a lower value of K could simultaneously decrease both the error and the simulation time. This shows the importance of monitoring the spectrum of $\mathbf{G}$ and $\mathbf{E}$ when selecting these parameters, as otherwise one could select a suboptimal combination. For larger values of M, i.e. > 13 for the ratios plotted in Fig. 4(b), this is no longer true and a smaller value of K will always result in a larger error.

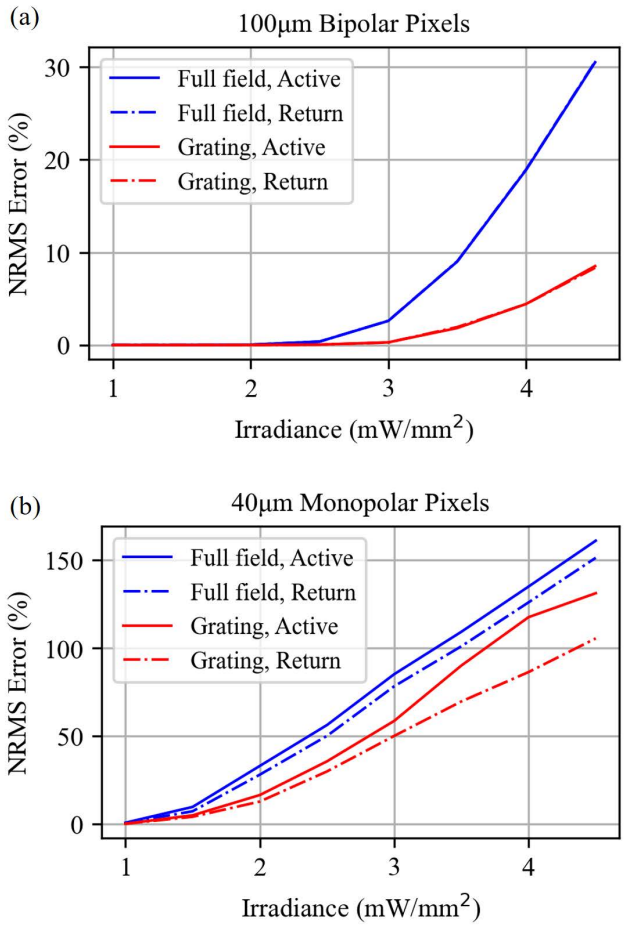

Fig. 7: Error introduced in the active and return electrodes by removing diodes from the circuit model, as a function of the illumination irradiance, with both full field and 1-pixel wide rectangular gratings for devices with (a) 100 µm bipolar pixels and (b) 40 µm monopolar pixels.

To calculate the actual error in electric current resulting from the thresholding and compensation described above, a Landolt C pattern with a 90 µm wide gap shown in Fig. 2(b) was projected at an irradiance level of $3\,\mathrm{mW/mm^2}$, with a pulse width of 9.8 ms, repeated at 30 Hz. The simulation was 330 ms long, enough time to allow convergence to steady state. The simulation was ran using the unmodified conductance matrix $\mathbf{G}$, an uncompensated sparse matrix $\mathbf{S}$, the sparse matrix with general compensation $\mathbf{S}_1$ and the sparse matrix with both general and image-specific compensation terms $\mathbf{S}_2$. For each case, the current injection from each pixel is found using RPSim, and then, with the unmodified (full) matrix serving as a benchmark, the relative error was calculated for both the 2-norm of currents from all pixels and the maximum current from all pixels. The results are shown in Fig. 5. Over the plotted window of the simulation, the average of the 2-norm of the relative error for the uncompensated sparse matrix is about 4.6%, while with the general compensation term this is reduced to 0.65%, and with the image-specific compensation - to 0.036%.

Additionally, to confirm the tractability of this method, the simulation was run with $M = 1$ and $\mathrm{K} = 0.1$ for various implant geometries – bipolar and monopolar devices including 100, 75, 40, and 20 µm pixel sizes. The number of pixels on these devices ranges from 205 to 2806. Bipolar devices have both an active and return electrode on every pixel, whereas monopolar devices have one shared return electrode along the edge of the device [6]. This means that bipolar devices have nearly twice as many electrodes, and therefore a 4x larger resistance mesh compared to a monopolar implant of the same dimensions. We can see in Fig. 6(a) that in all cases the computation time was reduced by the expected factor of 10, corresponding to the thresholding ratio. To enable simulation within a reasonable timeframe for larger implants with smaller pixels, the thresholding value can be reduced even further.

To evaluate performance of the algorithm with respect to the thresholding ratio, two additional patterns – first a full field illumination and second several Landolt Cs tiled on the implant (Fig. 6(b)) - were tested on a monopolar 40 µm array, at the same irradiance, frequency, and pulse width as the original pattern (Landolt C with a 90 µm gap size). The normalized root mean square (NRMS) error of the average current during an illumination pulse, as well as the simulation time are plotted for each pattern in Fig. 6(c) and (d), respectively. For all patterns tested, the error is less than 1% for all $\mathrm{K} > 0.05$. Additionally, for a simplification ratio of 0.1, the average error for the three patterns is 0.28%, with a corresponding average reduction of the simulation time of 89.5% (9.5x faster). If a lower error or faster simulation is desired, additional low-rank general compensation vectors of the error matrix should be included. The error associated with a specific thresholding ratio will vary with the number of compensation vectors M, as illustrated by Fig. 4(b). Additionally, because each illuminated pixel is a current source in the circuit simulation, larger patterns take longer to simulate – explaining the difference

in simulation time between patterns in Fig. 6(d). For all simulations, there are elements of computation that do not involve the resistance mesh. As such, there is a small offset in simulation time such that a sparsification ratio of $\mathrm{K} = 0$ will still have a nonzero simulation time. Nonetheless, it is clear from Fig. 6(d) that the computation time for this implant grows linearly with the simplification ratio K, which confirms the postulate that simulation speed is limited primarily by the size of the conductance matrix.

Furthermore, to illustrate the aforementioned ability of this algorithm to handle more extreme conditions, a larger bipolar implant with 20 µm pixels, having 7658 electrodes, was tested with the LDC pattern described earlier. With a netlist that itself is over 2GB involving nearly 59 million resistors, simulation of such a device without the techniques presented here would be impossible without access to extreme computational resources. With a 10x simplification slightly modified from that described above – $\mathrm{K} = 0.1$ and $M = 34$ – the simulation was completed in 28.41 hours. While this capability is encouraging, for iterative optimization of the device design, this is still prohibitively long. For further simplification a more optimal set of hyperparameters was found to be $\mathrm{K} = 0.025$ and $M = 200$. The runtime decreased an additional 34.22 times – down to 0.83 hours. The simulation with the full conductance matrix was not completed, but extrapolating the runtime by the number of electrodes would predict it to be around 111 hours. It is important to note that such extrapolation is inherently unreliable: for example, using the same extrapolation based on the simulations with 10 times simplified matrices predicts a runtime of 9.33 hours – a third of the observed 28.41 hours. Therefore, this is likely an overly conservative estimate, and even with that, this would imply a total speedup of 133 times. Similarly, the error with respect to the unmodified simulation is unknown; however, when compared to the simulation using $\mathrm{K} = 0.1$ and $M = 34$, the norm of the average deviation in electrode current was 3.88%.

Finally, To quantify the irradiances at which the reverse conduction through photodiodes can be neglected, a full field and grating patterns with 1-pixel wide bars were tested at 30 Hz with a pulse width of 9.8 ms. The average error (NRMS) in the calculated current, as previously defined, is shown for both the active and return electrodes as a function of irradiance in Fig. 7. The error is introduced once there is a significant voltage across a diode, such that it begins to conduct current. For PRIMA bipolar pixels, there are two photodiodes in series requiring twice the voltage before forward conduction begins. For this reason, the error at a given irradiance is lower for these pixels than for their monopolar counterparts. Additionally, the nominally small inter-pixel coupling for bipolar pixels results in close matching between the error in an active electrode and its local return electrode. This correlation becomes much more complicated for a monopolar design with just one global return electrode. Therefore, in monopolar devices, while the errors for the active and return electrodes do follow similar trends, they still differ significantly. For such reasons, the maximum irradiance introducing less than 1% error is dependent on the pattern and pixel design, but in the worst case for 100 µm PRIMA bipolar pixels this is $2.5\,\mathrm{mW/mm^2}$, while for a monopolar 40 µm device – it is $1.0\,\mathrm{mW/mm^2}$.

IV. Conclusions and Impact

By using a sparse approximation to the original conductance matrix along with a low rank compensation matrix that scales linearly with the number of pixels, we unlock the full potential of RPSim for modelling neurostimulating arrays, including the next generation of subretinal implants. We see that in practice, with realistic stimulation patterns and parameters mimicking what is used in clinical settings (letters and sparse bars), the error resulting from this simplification is negligible - well below 1%, while reducing the netlist size and computation time by nearly 10-fold. Further reductions in computational length are also feasible for simulations involving larger implants. Speeding up the computation so dramatically will enable the use of iterative optimization techniques for the design of multi-electrode arrays operating under various conditions. This is important as electrode design plays a crucial role in the selectivity and efficacy of neurostimulation implants. Improper electrode design can result in poor stimulation of neurons, low contrast of the patterns, or the undesired stimulation of non-target cells. Designing electrodes for selective stimulation of cells is the key to achieving high resolution prosthetic vision, as well as other high-fidelity electro-neural interfaces.

Acknowledgment

Authors declare no financial interest in the subject of this paper.

We would like to thank Yueming Zhuo and Ken Kundert for discussions on topics relevant to this paper.

References

[1] D. Palanker, Y. L. Mer, S. Mohand-Said, and J. Sahel, "Simultaneous perception of prosthetic and natural vision in amd patients," *Nature Communications*, vol. 13, no. 513, Jan. 2022. DOI: 10.1038/s41467-022-28125-x.

[2] D. Palanker, Y. L. Mer, S. Mohand-Said, M. Muqit, and J. Sahel, "Photovoltaic restoration of central vision in atrophic age-related macular degeneration," *Ophthalmology*, vol. 127, no. 8, pp. 1097–1104, Aug. 2020.

[3] B. Wang, Z. Chen, M. Bhuckory, *et al.*, "Electronic photoreceptors enable prosthetic vision with acuity matching the natural resolution in rats," *Nature Communications*, vol. 13, no. 6627, Nov. 2022.

[4] E. Ho, X. Lei, T. Flores, *et al.*, "Characteristics of prosthetic vision in rats with subretinal flat and pillar electrode arrays," *Journal of Neural Engineering*, vol. 16, no. 6, Oct. 2019. DOI: 10.1088/1741-2552/ab34b3.

[5] H. Lorach, G. Goetz, R. Smith, *et al.*, "Photovoltaic restoration of sight with high visual acuity," *Nature Medicine*, vol. 21, pp. 476–482, Apr. 2015. DOI: 10.1038/nm.3851.

[6] Z. Chen, B. Wang, A. Goldstein, E. Butt, K. Mathieson, and D. Palanker, "Photovoltaic implant simulator reveals resolution limits in subretinal prosthesis," *Journal of Neural Engineering*, vol. 19, no. 5, Sep. 27, 2022. DOI: 10.1088/1741-2552/ac8ed8.

[7] *Comsol multiphysics® v. 6.2*, https://www.comsol.com, COMSOL AB, Stockholm, Sweden, 2022.

[8] *Xyce™ parallel electronic simulator*, Computer software, Oct. 2013. DOI: 10.11578/dc.20171025.1421. [Online]. Available: https://github.com/Xycedev/Xyce.

[9] E. Keiter, T. Russo, R. Schiek, *et al.*, "Xyce™ parallel electronic simulator reference guide (v.7.4)," Tech. Rep., 2021, pp. 99–106. DOI: 10.2172/1826862.

[10] E. Keiter, R. Schiek, H. Thornquist, *et al.*, "Xyce™ parallel electronic simulator users' guide version 7.8," Tech. Rep., 2023, pp. 167–179.

[11] R. Telichevesky, K. Kundert, and J. White, "Efficient steady-state analysis based on matrix-free krylov-subspace methods," in *Proceedings of the 32nd Annual ACM/IEEE Design Automation Conference*, ser. DAC '95, New York, NY, USA: Association for Computing Machinery, 1995, pp. 480–484, ISBN: 0897917251. DOI: 10.1145/217474.217574.

[12] J. Newman, "Resistance for flow of current to a disk," *Journal of the Electrochemical Society*, vol. 113, no. 5, p. 501, 1966. DOI: 10.1149/1.2424003.

[13] D. Boinagrov, X. Lei, G. Goetz, *et al.*, "Photovoltaic pixels for neural stimulation: Circuit models and performance," *IEEE Transactions on Biomedical Circuits and Systems*, vol. 10, no. 1, pp. 85–97, Feb. 2016. DOI: 10.1109/TBCAS.2014.2376528.